metals

Article

Effect of Mg on Inclusion and High Cycle Fatigue Behavior in Titanium Microalloyed Beam Steel

Zhijun Gao [1,†], Guangfei Pan [1,†], Shuize Wang [1,2,*], Yu Song [3], Honghui Wu [1,2] and Xinping Mao [1,2]

[1] Beijing Advanced Innovation Center for Materials Genome Engineering, University of Science and Technology Beijing, Beijing 100083, China
[2] Guangdong Laboratory for Materials Science and Technology, Yangjiang Branch (Yangjiang Advanced Alloys Laboratory), Yangjiang 529500, China
[3] College of Material Science and Engineering, Chongqing University, Chongqing 400044, China
* Correspondence: wangshuize@ustb.edu.cn
† These authors contributed equally to this work.

Abstract: In this paper, the fatigue behavior of titanium microalloyed beam steels were studied by high cycle fatigue test and fatigue crack growth rate test. The effect of Mg addition on the fatigue behavior in titanium microalloyed beam steel was systematically analyzed. According to the experimental results, the addition of magnesium can effectively modify the inclusions by reducing the size of Al_2O_3 and TiN and promoting the formation of finer complex inclusions with a $MgO{\cdot}Al_2O_3$ core in titanium microalloyed high-strength beam steel. The number of inclusions in the experimental steels had far less of an impact on the fatigue characteristic than inclusion size. With the heterogeneous nucleation effect of $MgO{\cdot}Al_2O_3$, the inclusions are refined after the Mg addition. The tensile strength of Beam-2 steel decreased by approximately 54 MPa, while its fatigue strength increased by about 33 MPa, showing favorable fatigue resistance. These findings are essential for optimize the fatigue properties of titanium microalloy steel and promoting the development of automobile beam steel with excellent fatigue properties.

Keywords: titanium microalloyed steel; high cycle fatigue; fatigue fracture

Citation: Gao, Z.; Pan, G.; Wang, S.; Song, Y.; Wu, H.; Mao, X. Effect of Mg on Inclusion and High Cycle Fatigue Behavior in Titanium Microalloyed Beam Steel. *Metals* **2023**, *13*, 760. https://doi.org/10.3390/met13040760

Academic Editor: Alireza Akhavan-Safar

Received: 22 March 2023
Revised: 10 April 2023
Accepted: 12 April 2023
Published: 13 April 2023

1. Introduction

In light of the growing requirements of carbon-neutral development, the lightweight of automobiles has gradually attracted widespread attention from steel companies and automobile manufacturers [1–3]. Fatigue resistance is a key property related to the life-cycle sustainability of assemblies [4]. However, due to the complex mechanism of fatigue crack initiation and uncertain stress state, it is difficult to predict the fatigue resistance of assemblies.

Titanium (Ti) microalloyed beam steel is a high strength and toughness automotive structural steel, which is widely used in longitudinal and transverse beams and other parts of automobile frames [5–9]. The fatigue performance of key components is directly related to the fatigue resistance of assemblies. As an important load bearing part of automobile structure, the fatigue performance of automobile beam is particularly important. However, during the complex service environment, the beam steel is under complex and variable stress conditions for extended periods, making it prone to cause fatigue failure. Titanium microalloyed beam steel is guaranteed by the excellent precipitation strengthening effect of titanium. Although titanium microalloying technology has the advantages of low cost and obvious strengthening effect, the addition of titanium will inevitably form TiN, which is will seriously deteriorate the service performance of the material, especially reducing its fatigue life.

In general, inclusions inevitably exist in steel, and these inclusions have a direct impact on the fatigue life of the material [10–12]. During cyclic loading, hard and brittle inclusions

can easily to form microscopic cracks in steel, and gradually expand to form macroscopic cracks, resulting in fatigue failure. The physical properties (expansion coefficient, hardness, etc.) and the number, size, shape and other factors of inclusions will cause different degrees of the damage to fatigue performance [13–16]. Studies have shown that TiN with sharp shape and hard brittleness has 4 times more harmful effect on fatigue performance than spherical oxide inclusions [17–19].

However, the advances in oxide metallurgy technology have made it possible to improve the distribution of TiN in titanium microalloy steel and reduce its harmful effects on fatigue performance. It is found that the addition of magnesium (Mg) can change the type of inclusions, and effectively reduce the size of Al_2O_3 inclusions [20–23]. When magnesium is used in aluminum deoxidized steel, only magnesium aluminum spinel ($MgO{\cdot}Al_2O_3$) with a melting point of 2135 °C is produced, and this type of inclusion has a fine dispersion distribution compared to Al_2O_3 [24,25]. Additionally, it can also be used as a heterogeneous nucleation core of TiN during the solidification process, effectively reducing the size of TiN and improving the fatigue performance of steel [26,27].

In this paper, by analyzing and characterizing the microstructure, mechanical properties and fatigue properties of titanium microalloyed high strength beam steel, the mechanism of magnesium in improving the distribution characteristics was found out, and the high cycle fatigue properties and fatigue fracture mechanism of titanium microalloyed high strength beam steel were also investigated.

2. Materials and Methods

2.1. Experimental Materials

The experimental steels Beam-1 and Beam-2 were vacuum smelted to reduce the content of impurity elements. In order to study the modification effect of trace Mg element on inclusions, a small amount of Mg element is guaranteed by Ni-Mg intermediate alloy. The chemical compositions of the experimental steels are shown in Table 1, and the magnesium contents in the Beam-1 and Beam-2 samples were 0 and 0.0006 wt.%, respectively. The as-cast billet with 50 mm thickness was homogenized at 1250 °C for 60 min in preparation for hot rolling. The final rolling temperature was controlled at 850 °C, and then the rolled plate was air-cooled to room temperature. After hot rolling, a plate with a thickness of 8 mm was finally obtained. Figure 1 shows the microstructure of Beam-1 and Beam-2 steels, and both experimental steels are composed of ferrite and a small amount of pearlite because of the same composition system and preparation process.

Table 1. The chemical compositions of the experimental steels (wt.%).

Sample	C	Si	Mn	S	N	Nb	Ti	Al	O	Mg
standard	0.040–0.060	0.05–0.10	1.40–1.50	≤0.020	≤0.004	0.030–0.050	0.075–0.095	≤0.040	≤0.0030	-
Beam-1	0.060	0.06	1.49	0.004	0.0030	0.037	0.075	0.034	0.0022	0
Beam-2	0.034	0.07	1.50	0.005	0.0023	0.036	0.075	0.033	0.0028	0.0006

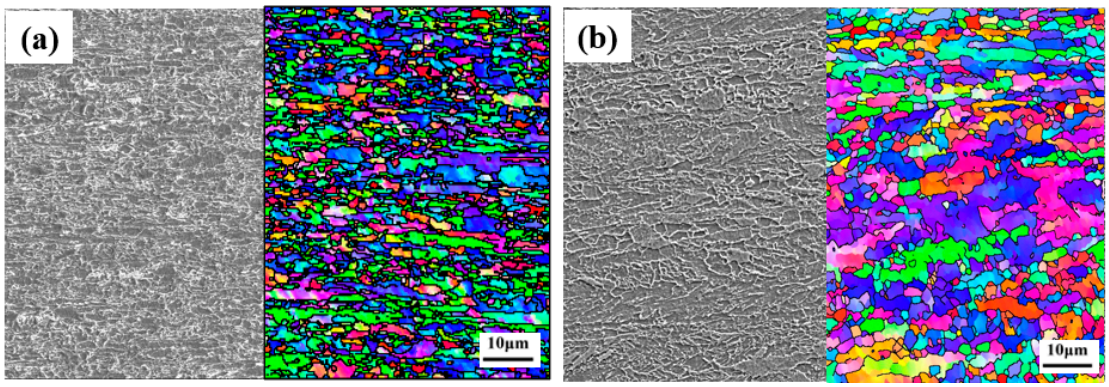

Figure 1. Microstructure of Beam-1 steel (**a**) and Beam-2 steel (**b**).

2.2. Characterization of the Inclusions

The characterization of the inclusions was conducted using an Aspex Explorer inclusion analyzer, and the scanning area was 19.3 mm^2. The sample for inclusion characterization was ground sequentially with 300 to 2000 grit SiC paper, and then mechanically polished with 2.5 μm diamond paste. A Phenom World BV scanning electron microscope (SEM) with energy dispersive spectroscopy (EDS) was used to obtain inclusion morphology and composition analysis.

2.3. Fatigue Testing and Fracture Observation

According to the GB/T 26076-2010 standard, the smooth high cycle fatigue (HCF) test was carried out on a QBG-50 fatigue testing machine, and 30 samples were randomly selected from different positions of the plate for experimental fatigue testing. Considering the service conditions of beam steel and experimental conditions, the axial tension test is adopted with a stress ratio R = 0.1. Loading force form is sinusoidal waveform for all fatigue test. The experiment ends when the sample breaks or the number of cycles reaches 10^7. In order to improve the fatigue data confidence, the fatigue limit $\sigma_{0.1}$ is measured by the step method. The HCF experiment takes 3 to 5 stress levels, and the stress increment of each level is about 3% of the fatigue limit $\sigma_{0.1}$. To minimize the effect of surface roughness, the surfaces of all specimens were polished in the axial direction with 600 to 1500 grit paper. After the fatigue specimen fractured, a Zeiss Evo18 SEM was used to observe the fatigue fracture, and the composition of inclusions at the fracture was analyzed by EDS analyzer. The fatigue crack growth (FCG) rate test was performed using a standard compact tension (CT) specimen (W = 40 mm) according to GB/T 6398-2017. The geometry and dimensions of HCF test specimen and FCG growth test specimen used in the present study is shown in Figure 2. The thickness of the specimens for fatigue test and fatigue crack growth rate test are both 4 mm.

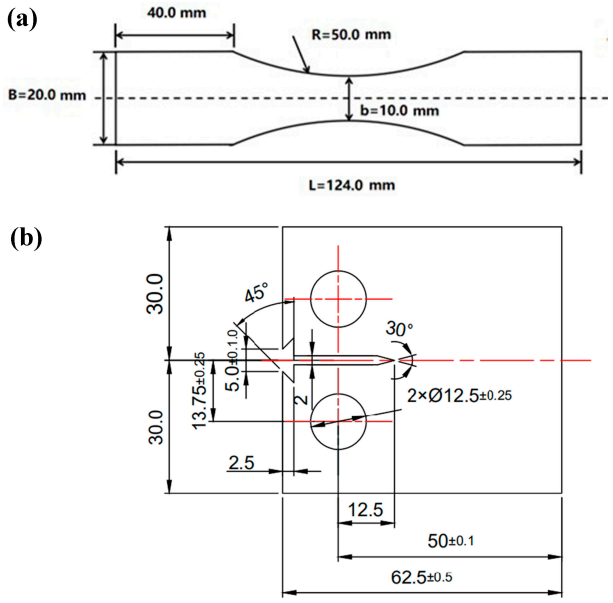

Figure 2. Geometry and dimensions of high cycle fatigue test specimen (**a**) and fatigue crack growth rate test specimen (**b**).

3. Results and Discussion

3.1. Effect of Mg on the Composition and Morphology of Inclusions

In order to analyze the modification effect of inclusions in the experimental steels after Mg addition, the quantitative analysis results of Mg, Al and Ti in as inclusions of Beam-1 and Beam-2 steels are listed, as shown in Figure 3. According to Figure 3a,b, the average content of Mg, Al and Ti in Beam-1 steel is 1.9%, 33.8% and 64.3%, and the average

contents of Mg, Al and Ti elements in Beam-2 steel are 14.6%, 55.1% and 30.3%, respectively. The results show that complex inclusions mainly composed of Ti and Al are primarily formed in Beam-1 steel because of the relatively high Ti content and low Mg content. In the Beam-2 steel, due to the addition of Mg, the content of the Mg has increased significantly in complex inclusion, indicating that the inclusion types have changed.

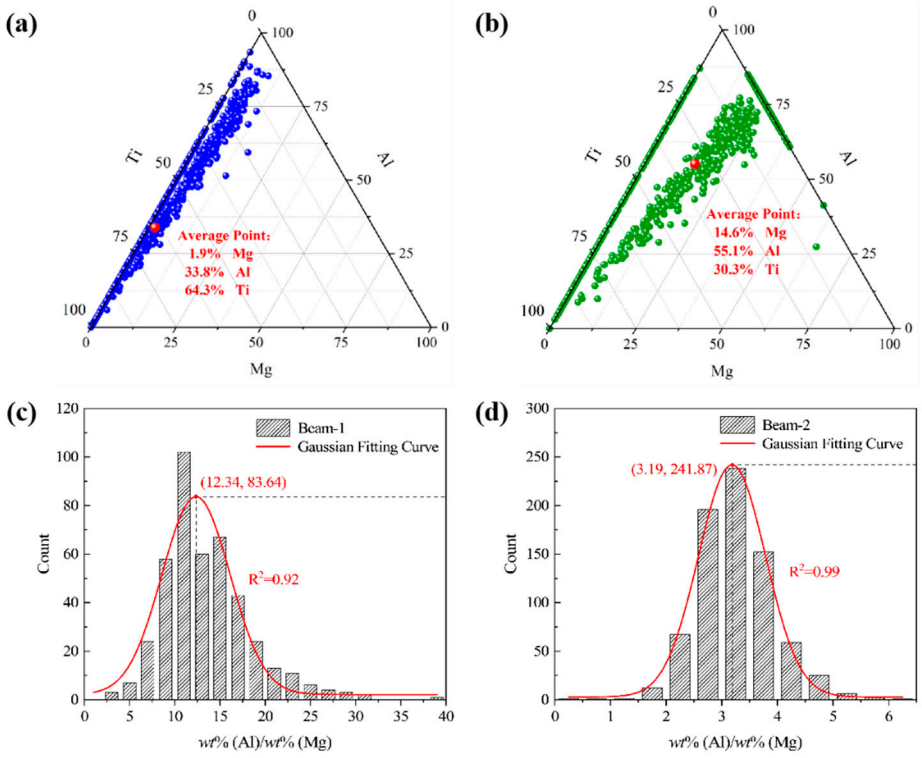

Figure 3. Composition distribution characteristics of the inclusions in Beam-1 steels (**a**) and Beam-2 steel (**b**); statistical histogram of Al/Mg mass ratio of (Al, Mg) Ti inclusions in Beam-1 steel (**c**) and Beam-2 steel (**d**).

Figure 3c,d shows the statistical histogram of the Al/Mg mass ratio of (Al, Mg) Ti inclusions in the Beam-1 and Beam-2 steel. It can be seen that the Al/Mg mass ratio of the inclusions in the Beam-1 steel is concentrated in the range of 8–18. According to Gaussian fitting, the average Al/Mg mass ratio is calculated to be 12.34, and the Al content in the inclusions was far greater than the Mg content. After Mg addition, the Al/Mg mass ratio of the precipitates in Beam-2 steel gradually decreases, and is mainly distributed in the range of 2.5–4.0. Gaussian fitting result shows that the average Al/Mg mass ratio in Beam-2 steel is 3.19, which is much smaller than that of Beam-1 steel. It should be noted that the trace amount of Mg in the inclusions of Beam-1 steel mainly came from refractory materials during the smelting process [28].

In order to compare the inclusion characteristics, the morphology and EDS spectrum of Beam-1 and Beam-2 steels are obtained respectively. Due to the differences in the chemical composition and structure, inclusions were divided into two types: TiN inclusions and TiN complex inclusions with an oxide core. For the second type of complex inclusion, the core oxide changes simultaneously with the increase of Mg content. Figure 4a–c shows the typical inclusion morphology in Beam-1 steel, and Figure 4d shows the chemical composition of the corresponding inclusions, as marked by red arrow. In Figure 4a, the inclusions are mainly composed of two parts, the darker color area in the center and the lighter color area in the outer shell. According to the EDS results in Figure 4d, it can be seen that the dark part of the center of the complex inclusion is composed of Al, Ca and O, and the gray part of the shell is mainly composed of Ti, Nb, Fe and other elements. Figure 4e shows the detailed characteristics of the typical core-shell inclusion. It can be

clearly seen that the core is mainly composed of oxide inclusions containing Al, Ca, O and other elements, and the outer shell is mainly TiN.

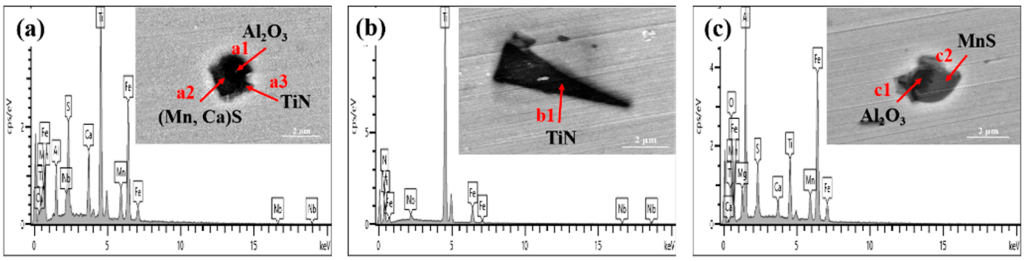

(d)

element (wt.%)	N	O	Al	Ca	Ti	Mn	S	Mg	Fe	Nb
a1	--	33.45	28.70	7.94	5.71	5.78	5.97	2.89	9.57	--
a2	--	--	6.89	17.15	3.74	21.99	20.12	0.66	29.45	--
a3	--	--	5.50	6.88	32.39	8.83	7.04	--	35.19	4.17
b1	18.12	1.33	--	--	69.84	--	--	--	10.11	1.92
c1	--	22.48	18.70	1.44	8.05	5.70	3.54	3.14	36.95	--
c2	--	--	--	3.55	2.77	27.78	16.76	--	46.47	--

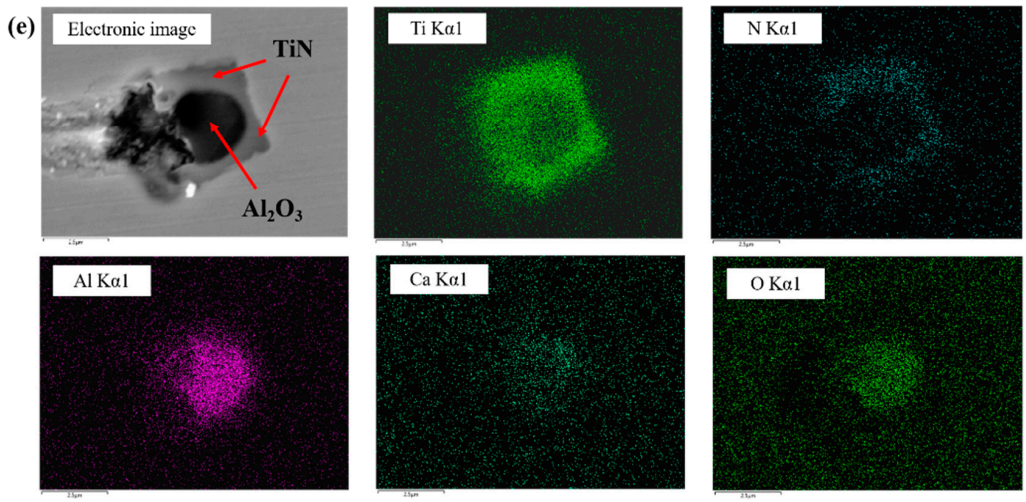

Figure 4. Morphological characteristics of inclusions in Beam-1 steel. (**a**–**c**) typical inclusion morphology; (**d**) chemical composition of the corresponding inclusions; (**e**) detailed characteristics of the typical core-shell inclusion.

Figure 5a–c shows the typical inclusions in Beam-2 steel. The morphological characteristics of inclusions are similar to those in Beam-1 steel. However, according to the EDS analysis results of the inclusions, it was found that the core of the complex inclusions was composed of Mg-Al oxide, as shown in Figure 5d, which shows the results of the contents of different elements at different positions of the complex inclusions. However, the morphology of complex inclusions is significantly different. Compared with the spherical inclusions in Figure 5b, the inclusions in Figure 5a are angular with sharp corner, resulting in stress concentration during, which could seriously deteriorate the fatigue property.

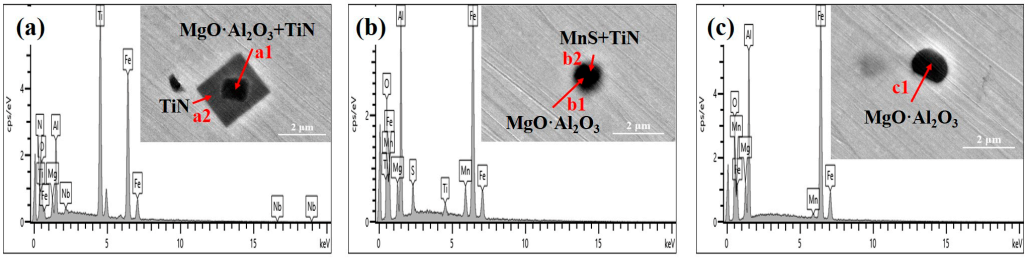

(d)

element (wt.%)	N	O	Al	Ca	Ti	Mn	S	Mg	Fe	Nb
a1	7.39	20.04	6.65	--	26.75	--	--	1.89	36.53	0.76
a2	13.95	--	0.53	--	34.03	0.86	--	--	50.63	--
b1	--	21.24	23.01	--	0.95	1.53	0.42	4.92	47.94	--
b2	--	18.47	18.17	--	1.21	5.83	2.23	3.78	50.31	--
c1	--	17.27	18.54	--	--	0.92	--	4.48	58.79	--

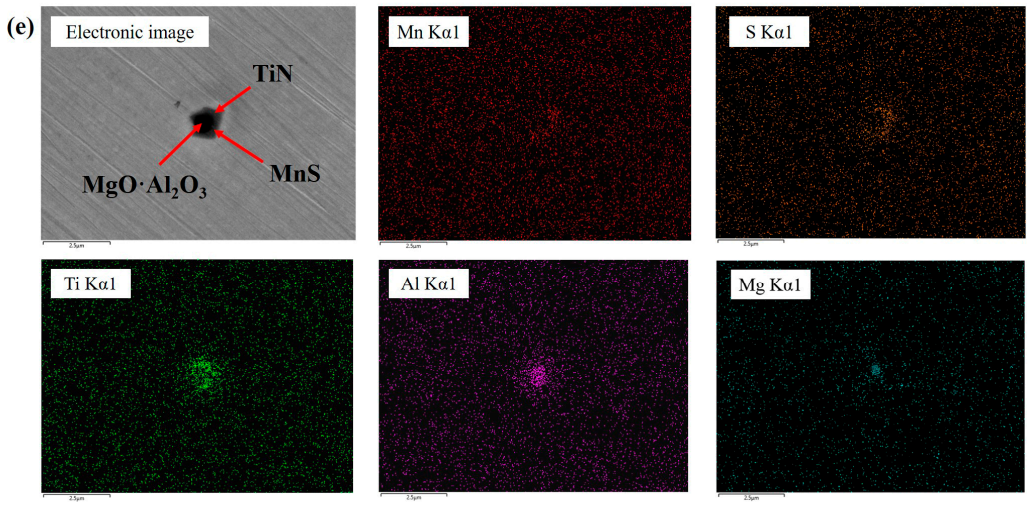

Figure 5. Morphological characteristics of inclusions in Beam-2 steel. (**a**–**c**) typical inclusion morphology; (**d**) chemical composition of the corresponding inclusions; (**e**) detailed characteristics of the typical core-shell inclusion.

Figure 5c shows typical inclusions in steel after Mg addition. Figure 5e shows the detailed characteristics of the typical core-shell inclusion with higher Mg content. The core of the inclusions is $MgO{\cdot}Al_2O_3$. Obviously, the size of the inclusions in Beam-1 steel is significantly larger than that of the inclusions in Beam-2 steel. Most notably, the inclusions with $MgO{\cdot}Al_2O_3$ cores are significantly smaller in size than those with Al_2O_3 cores.

3.2. Effect of Mg on Size and Quantity of Inclusions

Figure 6 shows comparison of inclusion distribution in Beam-1 and Beam-2 steels. It is clearly that there were fewer large-size inclusions in the observation area, and the inclusion distribution is more diffuse after the Mg addition.

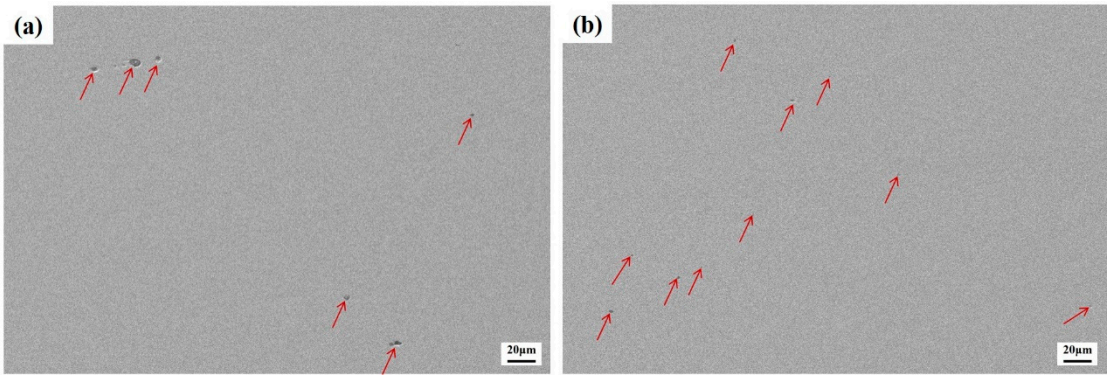

Figure 6. Comparison of inclusion distribution in Beam-1 (**a**) and Beam-2 (**b**) steels. The inclusion is marked by the red arrow.

Figure 7 shows inclusion distribution characteristics in the experimental steels. In order to improve the reliability of data statistics, the number of inclusions in the same scanning area of the experimental steels was counted separately. The effective inclusion numbers of the Beam-1 and Beam-2 experimental steels are 951 and 1100, respectively. As shown in Figure 7a, the total number of inclusions in the scanning area of Beam-1 steel is significantly less than that of Beam-2 steel, while the total area of inclusions is twice that of the inclusions in Beam-2 steel. Figure 7b shows the relationship between the area distribution and number of inclusions in experimental steels. The inclusion area in Beam-1 steel is mostly distributed in the range of 0–10 μm^2, while the inclusion area in Beam-2 steel is mainly distributed in the range of 0–5 μm^2. In addition, the inclusions with an area greater than 5 μm^2 in Beam-2 steel are less than those in the Beam-1 steel.

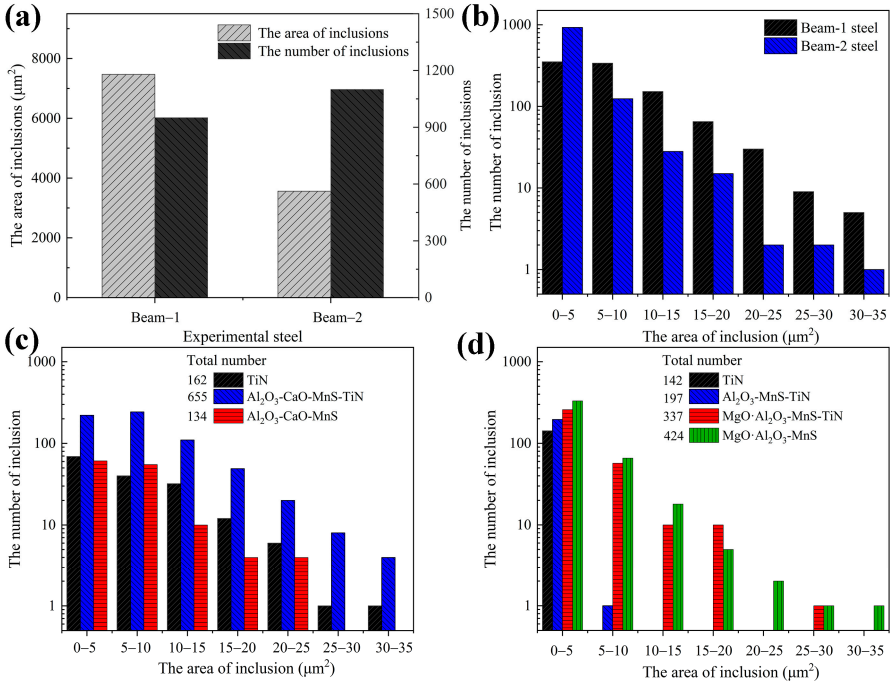

Figure 7. Inclusion number and area distribution in experimental steels: (**a**) total area and number of inclusions, (**b**) inclusion area distribution; (**c**) different types of inclusions in Beam-1 steel, (**d**) different types of inclusions in Beam-2 steel.

Figure 7c,d show the area distributions of different types inclusions in Beam-1 and Beam-2 steels, respectively. Figure 7c shows that the inclusions in Beam-1 steel can be divided into three types: TiN, Al_2O_3-CaO-MnS-TiN and Al_2O_3-CaO-MnS, and the total

number of the three types of inclusions is 162, 655, and 134, respectively. Among the three types of inclusions, Al_2O_3-CaO-MnS-TiN inclusions have the largest distribution range and the largest number in each area. Due to the addition of Mg, the types of inclusions in Beam-2 steel are divided into four types: TiN, Al_2O_3-MnS-TiN, $MgO{\cdot}Al_2O_3$-MnS-TiN and $MgO{\cdot}Al_2O_3$-MnS. The numbers of the four types of inclusions are 142, 197, 337 and 424, respectively. It can be seen that the distribution of inclusions in Beam-2 is more diffuse and finer, and the number of TiN is significantly reduced.

Generally, TiN inclusions with sharp corners have a small radius of curvature leading to serious stress concentration [29]. Microcracks are easy to initiate at the interface between TiN and matrix during cyclic loading. Under alternating stress, the cracks preferentially propagate along the vertical direction of the tensile stress, leading to final fracture [30]. Therefore, the reduction of TiN inclusions is very beneficial to improve the fatigue resistance of the experimental steels. In addition, a small amount of Mg transforms regular and clustered Al_2O_3 inclusions into diffusely distributed $MgO{\cdot}Al_2O_3$, which increases its nucleation rate and reduces the size of various oxide inclusions in the experimental steel. More importantly, according to the interface coherence theory, when the lattice structure of the heterogeneous phase is similar to that of the melt, and the interface between the heterogeneous phase and the melt has a low surface free energy, the heterogeneous phase can effectively promote the melt nucleation [31]. Based on Bramfitt's calculation model, it can be seen that the lattice misfit between $MgO{\cdot}Al_2O_3$ and TiN is 5.02%, and the mismatch of less than 12% is the effective nucleation range [32,33]. During the solidification process, $MgO{\cdot}Al_2O_3$ in molten steel can be used as the heterogeneous nucleation core of TiN to increase the nucleation rate of TiN and avoid the formation of large-sized TiN. Therefore, through the addition of a small amount of Mg, not only the Al_2O_3 in the steel is refined, but also the formation of large-sized TiN is suppressed.

3.3. Effect of Mg on Fatigue Properties

Figure 8a shows the high-cycle fatigue strength of the experimental steels tested by the staircase method. According to GBT 24147-2009, the fatigue limit strength (10^7 cycles) of Beam-1 and Beam-2 steels are determined. The stress amplitude interval is 10 MPa in this work. If fatigue failure occurs before the sample reaches 10^7 cycles, the next sample is tested at a lower stress amplitude. The results show that the fatigue strength of Beam-1 steel and Beam-2 steel are 643 MPa and 676 MPa, respectively. Based on the fatigue strength, the least square method is used to fit the HCF test data and the fatigue strength to obtain S-N curves of experimental steels, as shown in Figure 8b. It can be seen that under the same stress amplitude, the fatigue life of Beam-2 steel is significantly higher than that of Beam-1 steel.

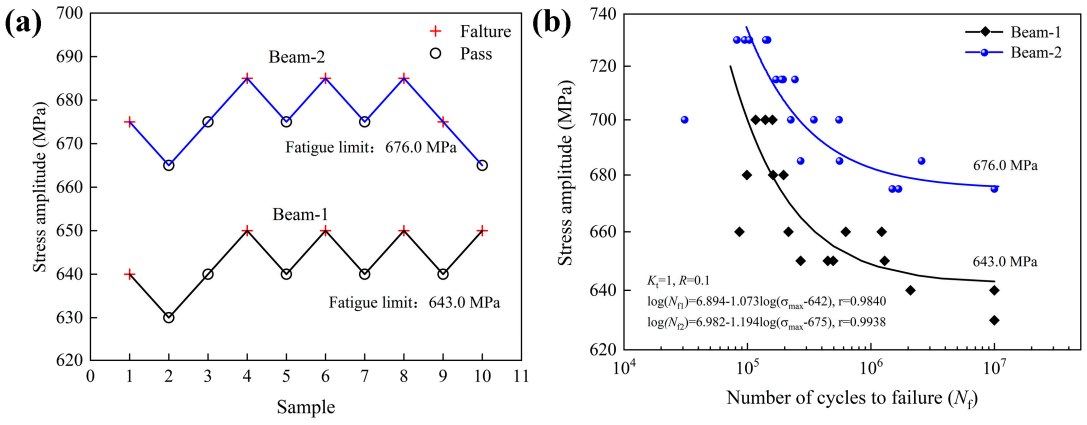

Figure 8. Fatigue strength results obtained by staircase method (**a**) and S-N curves (**b**).

Figures 9 and 10 shows the fatigue fracture of Beam-1 and Beam-2 steel respectively. The fracture morphology shows typical fatigue fracture characteristics in both steels, in-

cluding fatigue crack initiation area, fatigue crack stable propagation area and fatigue crack instability propagation area [34]. Inclusions were observed in the fatigue crack initiation area of both experimental steels, whereas the inclusion size in the fatigue crack initiation area of Beam-1 steel is significantly larger than that of Beam-2 steel. Comparing the fatigue crack stable propagation area, it is found that a large number of secondary microcracks and fatigue striations are observed in the direction perpendicular to the primary crack growth direction in the two experimental steels. During the cyclic loading, the crack tip is in a complex stress state. Under the action of dislocation movement and deformation energy storage, the main crack branches and forms discontinuously distributed secondary cracks in fatigue stable crack propagation stage.

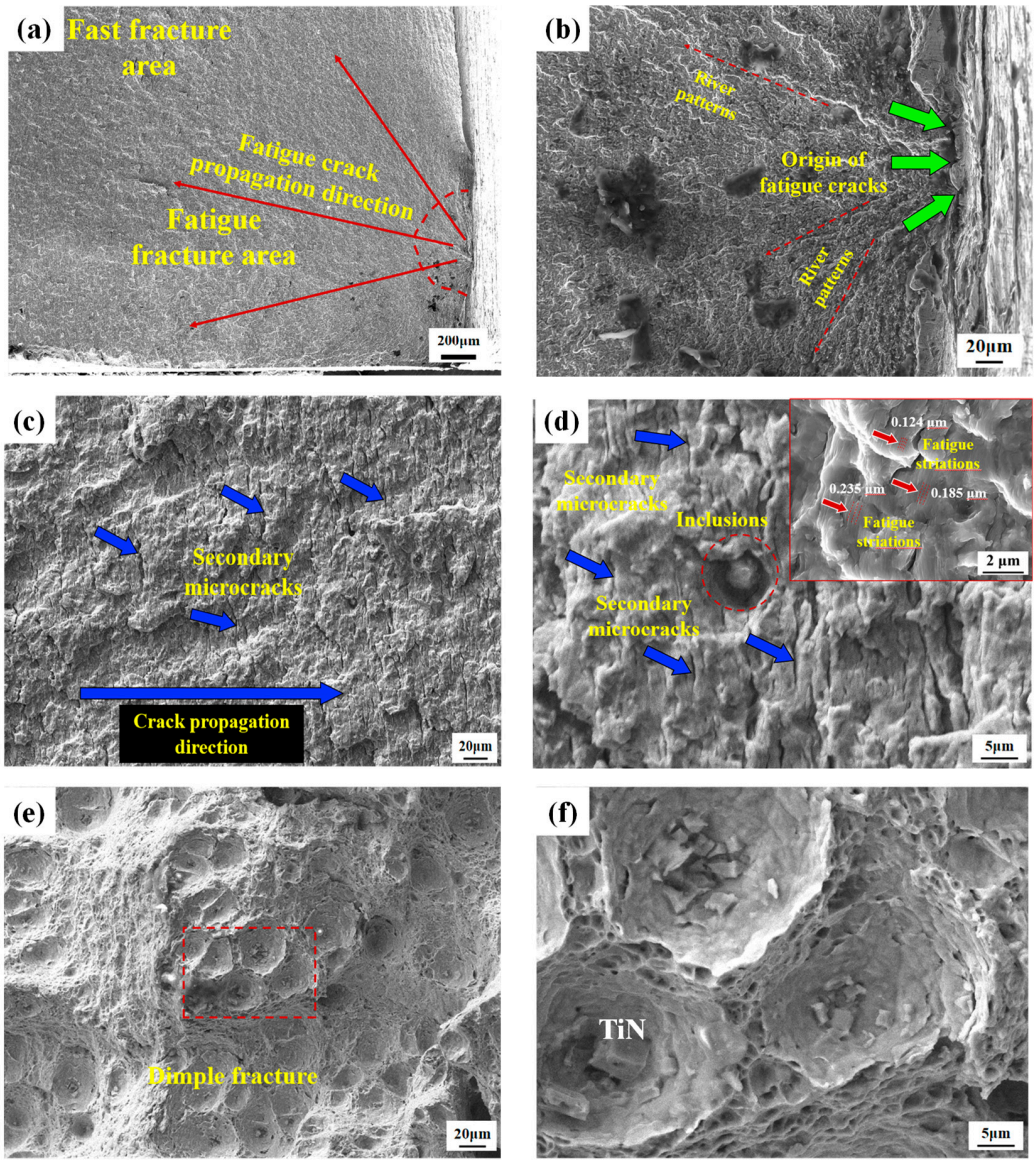

Figure 9. Fatigue fracture morphology of Beam-1 Steel, σ_a = 630 MPa, $N_f = 6.28 \times 10^5$: (**a**,**b**) fatigue crack initiation area, (**c**,**d**) fatigue crack stable propagation area, (**e**,**f**) fatigue crack instability propagation area.

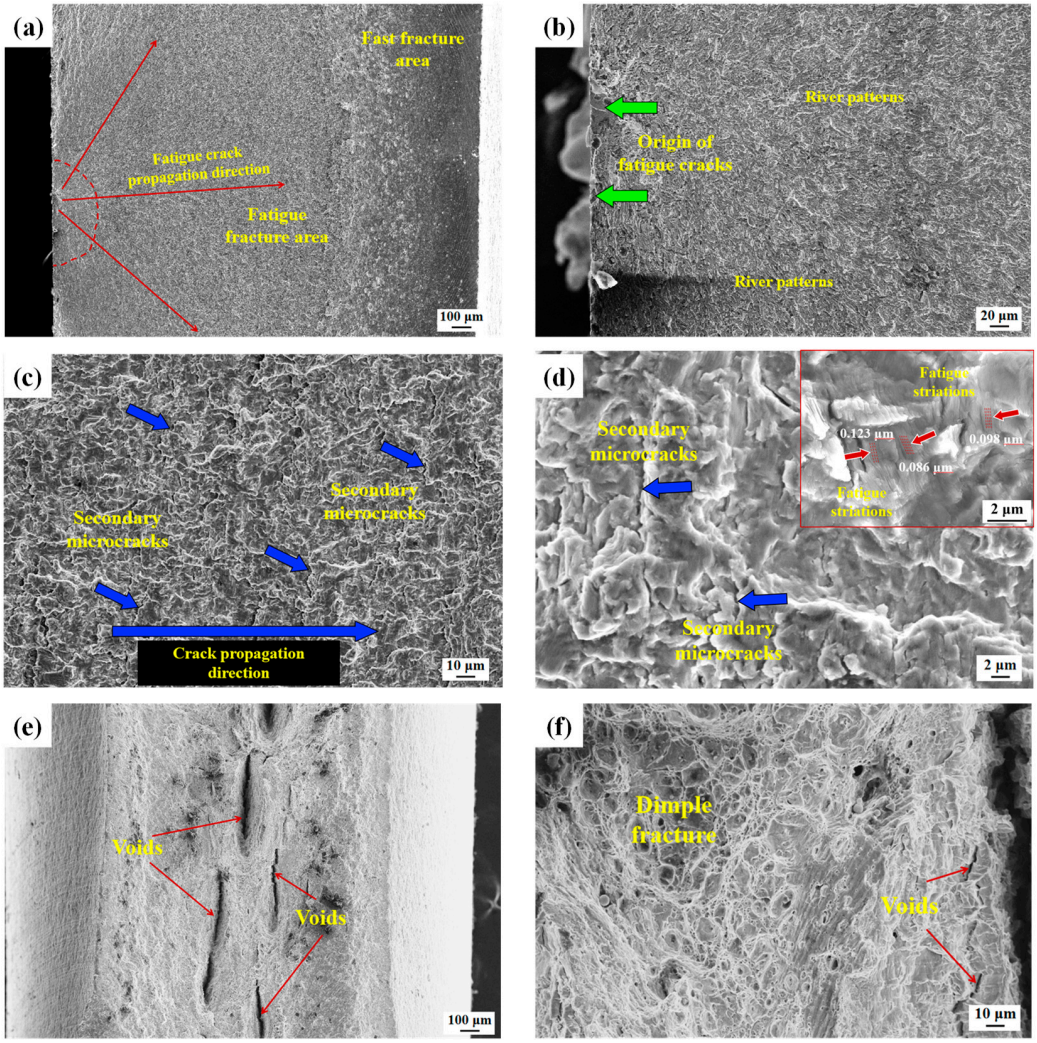

Figure 10. Fatigue fracture morphology of Beam-2 Steel, σ_a = 685 MPa, $N_f = 2.7 \times 10^5$: (**a**,**b**) fatigue crack initiation area, (**c**,**d**) fatigue crack stable propagation area, (**e**,**f**) fatigue crack instability propagation area.

By comparing the fatigue striation spacing in the fatigue stable crack propagation area, as shown in Figures 9d and 10d, it is found that the spacing of fatigue striation in Beam-2 steel is smaller than that of Beam-1 steel, indicating lower fatigue crack growth rate and higher fatigue resistance of Beam-2 steel. Beam-1 steel also found complex inclusions in the fatigue stable crack propagation area and instability propagation area, which will accelerate the fatigue crack growth rate. It is worth noting that the morphology of the instability propagation area is mainly composed of dimples in both experimental steels, which is a typical characteristic of ductile fracture. Additionally, because of the higher fatigue strength, Beam-2 steel exhibits better fatigue resistance. The dimples are connected to each other and coalesce into elongated voids during cyclic loading process, as shown in Figure 10e.

Generally, there is a simple proportional relationship between the fatigue strength and tensile strength of materials [35,36]. However, the opposite phenomenon appears in the experimental steels, as shown in Table 2. Due to the lower carbon content, the precipitation of carbides is reduced, resulting in a decrease in the strength of Beam-2 steel, which main strengthening mechanism is precipitation strengthening. Although Beam-2 steel has lower strength, it has higher fatigue strength, which is ~5% higher than that of Beam-1 steel. It is worth mentioning that the fatigue strength of Beam-2 steel is higher than the yield strength. Because of the lower stress ratio, the minimum stress amplitude is relatively low during

cyclic loading process, leading to a small cyclic plastic deformation region at the crack tip. On the other hand, the fatigue strength takes into account the effects of cyclic loading and crack growth on the material's strength, while the yield strength only refers to the point at which the material undergoes plastic deformation under a steady-state load. As a result, the relatively low degree of cyclic plastic deformation can lead to slower crack growth rates and higher fatigue strength, which may exceed its yield strength. Similar fatigue test results have been reported in related research at a small stress ratio [37,38].

Table 2. Mechanical properties and fatigue strength of Beam-1 and Beam-2 steels (MPa).

Type	Tensile Strength Rm	Yield Strength $R_{p0.2}$	Fatigue Strength
Beam-1	740	674	643
Beam-2	686	634	676

Studies have shown that defect characteristics in materials have a significant impact on fatigue life, such as size effect and defect location [39,40]. By comparing the inclusion distribution characteristics and fatigue properties of the experimental steels, it can be found that the inclusions size has a greater impact on the fatigue properties than the inclusion number. The fatigue strength of the experimental steel increases significantly with the decrease of inclusion size. After Mg addition, the Mg element fully modifies the Al_2O_3 that is easy to cluster, forming fine and dispersed $MgO{\cdot}Al_2O_3$. Furthermore, based on the good lattice matching, $MgO{\cdot}Al_2O_3$ can act as the heterogeneous nucleation core, which improves the distribution of TiN in terms of quantity and size. By minimizing the size of inclusions, the adverse effect of inclusions on fatigue property is reduced and the fatigue strength is increased in Beam-2 steel.

3.4. Effect of Mg on Fatigue Crack Growth

The fatigue life is mainly composed fatigue crack initiation life and fatigue crack growth life. Smaller inclusions can effectively reduce the stress concentration effect during cyclic loading, delay the initiation of fatigue cracks, and improve the fatigue life of materials [41]. Figure 11 shows the fatigue crack growth (FCG) rate results for Beam-1 and Beam-2 steels. In order to analyze the FCG behavior in mediate rate region, the Paris model is used to describe the relationship between the crack growth rate da/dN and the stress intensity factor ΔK [42,43]. The fitting curves by the Paris model of Beam-1 steel and Beam-2 steel are as follows:

$$da/dN = 7.23 \times 10^{-8} (\Delta K)^{2.41}, R^2 = 0.93, \quad (1)$$

$$da/dN = 4.58 \times 10^{-8} (\Delta K)^{2.52}, R^2 = 0.94, \quad (2)$$

where R^2 is the correlation coefficient.

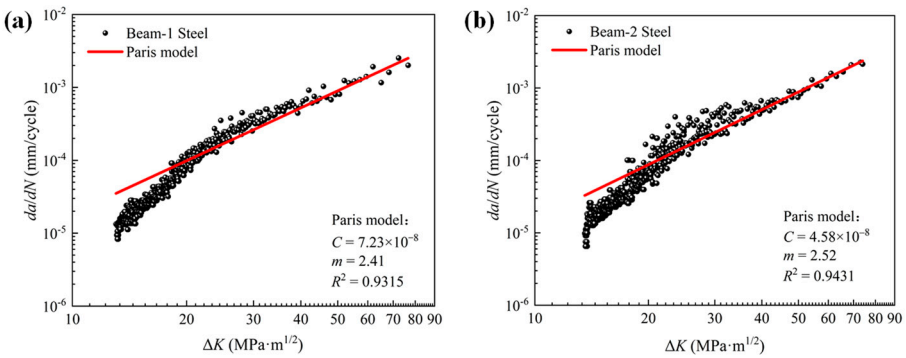

Figure 11. FCG experimental results and Paris model fitting results, (**a**) Beam-1 steel, (**b**) Beam-2 steel.

In the Paris model, m represents the slope of the fitting curve in the double logarithmic coordinates, which is inversely proportional to the FCG rate. According to the fitting results, the m values of Beam-1 and Beam-2 steels are 2.41 and 2.52, respectively. Therefore, the FCG rate of Beam-1 steel is the higher than that of Beam-2 steel, which has better resistance to crack propagation due to homogeneous microstructure. This result is also consistent with the observation in the fatigue stable crack propagation area. The fatigue striation distribution is more compact in Beam-2 steel.

4. Conclusions

In this paper, the fatigue behavior of titanium microalloyed beam steel was studied by HCF test and FCG rate test. In addition, the effect of Mg addition on the fatigue behavior was systematically analyzed, the main findings are summarized as follows:

(1) The addition of Mg can effectively modify the inclusions in the titanium microalloyed high-strength beam steel. The Al_2O_3 in the experimental steel is modified to $MgO{\cdot}Al_2O_3$ under the aluminum deoxidation conditions.

(2) After the addition of Mg, the area of inclusions decreased and the number density increased, in particular, the proportion of inclusions with an area less than 5 μm^2 increased significantly. The addition of Mg greatly reduced the size of Al_2O_3 and TiN, and promoted the formation of finer complex inclusions with a $MgO{\cdot}Al_2O_3$ core.

(3) The effect of the inclusion size on the fatigue property is much greater than the inclusion number of the experimental steels. After the Mg addition, the inclusions are refined through the heterogeneous nucleation effect of $MgO{\cdot}Al_2O_3$. The fatigue strength of Beam-2 steel increased by approximately 33 MPa despite a decrease in tensile strength of approximately 54 MPa.

Author Contributions: Conceptualization, Y.S.; methodology, S.W.; software, H.W.; validation, X.M., S.W. and H.W.; formal analysis, S.W.; investigation, Y.S.; resources, Y.S.; data curation, Z.G.; writing—original draft preparation, Z.G. and G.P.; writing—review and editing, Z.G. and G.P.; visualization, Z.G. and G.P.; supervision, S.W.; project administration, X.M. and S.W.; funding acquisition, Z.G. All authors have read and agreed to the published version of the manuscript.

Funding: This research was funded by National Natural Science Foundation of China, grant number No. 52104369 and China Postdoctoral Science Foundation, grant number No. 2021M700374.

Institutional Review Board Statement: Not applicable.

Informed Consent Statement: Informed consent was obtained from all subjects involved in the study.

Data Availability Statement: The data presented in this study are available on request from the corresponding author.

Conflicts of Interest: The authors declare no conflict of interest.

References

1. Wang, P.; Ryberg, M.; Yang, Y.; Feng, K.; Kara, S.; Hauschild, M.; Chen, W.Q. Efficiency stagnation in global steel production urges joint supply-and demand-side mitigation efforts. *Nat. Commun.* **2021**, *12*, 2066. [CrossRef] [PubMed]
2. Wolfram, P.; Weber, S.; Gillingham, K.; Hertwich, E.G. Pricing indirect emissions accelerates low-carbon transition of US light vehicle sector. *Nat. Commun.* **2021**, *12*, 7121. [CrossRef] [PubMed]
3. Agarwal, J.; Sahoo, S.; Mohanty, S.; Nayak, S.K. Progress of novel techniques for lightweight automobile applications through innovative eco-friendly composite materials: A review. *J. Thermoplast. Compos.* **2020**, *33*, 978–1013. [CrossRef]
4. Wang, S.; Gao, Z.; Wu, G.; Mao, X. Titanium microalloying of steel: A review of its effects on processing, microstructure and mechanical properties. *Int. J. Min. Met. Mater.* **2022**, *29*, 645–661. [CrossRef]
5. Bai, Y.; Nardi, D.C.; Zhou, X.; Picón, R.A.; Flórez-López, J. A new comprehensive model of damage for flexural subassemblies prone to fatigue. *Comput. Struct.* **2021**, *256*, 106639. [CrossRef]
6. Mao, X. *Titanium Microalloyed Steel: Fundamentals, Technology*, 1st ed.; Springer: Berlin/Heidelberg, Germany, 2019; pp. 1–34.
7. Zhang, Q.; Huo, X.; Li, L.; Chen, S.; Lu, C. Correlation between Precipitation and Recrystallisation during Stress Relaxation in Titanium Microalloyed Steel. *Metals* **2022**, *12*, 1920. [CrossRef]

8. Tang, S.; Li, X.; Li, J.; Liu, Z.; Wang, G. Role of Microalloying Elements on Recrystallization Kinetics of Cold-Rolled High Strength Low Alloy Steels. *Metals* **2022**, *12*, 1741. [CrossRef]
9. Zhang, Z.; Wang, Z.; Li, Z.; Sun, X. Microstructure Evolution and Precipitation Behavior in Nb and Nb-Mo Microalloyed Fire-Resistant Steels. *Metals* **2023**, *13*, 112. [CrossRef]
10. Zerbst, U.; Madia, M.; Klinger, C.; Bettge, D.; Murakami, Y. Defects as a root cause of fatigue failure of metallic components. I: Basic aspects. *Eng. Fail. Anal.* **2019**, *97*, 777–792. [CrossRef]
11. Zerbst, U.; Madia, M.; Klinger, C.; Bettge, D.; Murakami, Y. Defects as a root cause of fatigue failure of metallic components. II: Non-metallic inclusions. *Eng. Fail. Anal.* **2019**, *98*, 228–239. [CrossRef]
12. Zhu, M.L.; Jin, L.; Xuan, F.Z. Fatigue life and mechanistic modeling of interior micro-defect induced cracking in high cycle and very high cycle regimes. *Acta Mater.* **2018**, *157*, 259–275. [CrossRef]
13. Murakami, Y. Effects of small defects and nonmetallic inclusions on the fatigue strength of metals. *JSME Int. J. Ser. 1 Solid Mech. Strength Mater.* **1989**, *32*, 167–180. [CrossRef]
14. Murakami, Y.; Kodama, S.; Konuma, S. Quantitative evaluation of effects of non-metallic inclusions on fatigue strength of high strength steels. I: Basic fatigue mechanism and evaluation of correlation between the fatigue fracture stress and the size and location of non-metallic inclusions. *Int. J. Fatigue* **1989**, *11*, 291–298. [CrossRef]
15. Scorza, D.; Carpinteri, A.; Ronchei, C.; Vantadori, S.; Zanichelli, A. Effect of non-metallic inclusions on AISI 4140 fatigue strength. *Int. J. Fatigue* **2022**, *163*, 107031. [CrossRef]
16. Sun, C.; Lei, Z.; Xie, J.; Hong, Y. Effects of inclusion size and stress ratio on fatigue strength for high-strength steels with fish-eye mode failure. *Int. J. Fatigue* **2013**, *48*, 19–27. [CrossRef]
17. Wang, P.; Wang, B.; Liu, Y.; Zhang, P.; Luan, Y.K.; Li, D.Z.; Zhang, Z.F. Effects of inclusion types on the high-cycle fatigue properties of high-strength steel. *Scr. Mater.* **2022**, *206*, 114232. [CrossRef]
18. Yang, Z.G.; Zhang, J.M.; Li, S.X.; Wang, Q.Y.; Hui, W.J.; Weng, Y.Q. On the critical inclusion size of high strength steels under ultra-high cycle fatigue. *Mat. Sci. Eng. A* **2006**, *427*, 167–174. [CrossRef]
19. Beretta, S.; Anderson, C.; Murakami, Y. Extreme value models for the assessment of steels containing multiple types of inclusion. *Acta Mater.* **2006**, *54*, 2277–2289. [CrossRef]
20. Liu, F.; Li, J.; Wang, Q.; Liu, Y.; Bai, Y.; He, T.; Yuan, G. Microstructural refinement by the formation of acicular ferrite on Ti–Mg oxide inclusion in low-carbon steel. *Mat. Sci. Eng. A* **2021**, *824*, 141795. [CrossRef]
21. Guo, H.; Yang, S.; Wang, T.; Yuan, H.; Zhang, Y.; Li, J. Microstructure evolution and acicular ferrite nucleation in inclusion-engineered steel with modified MgO@ C nanoparticle addition. *J. Mater. Sci. Technol.* **2022**, *99*, 277–287. [CrossRef]
22. Kimura, K.; Fukumoto, S.; Shigesato, G.; Takahashi, A. Effect of Mg addition on equiaxed grain formation in ferritic stainless steel. *ISIJ Int.* **2013**, *53*, 2167–2175. [CrossRef]
23. Guo, H.; Yang, S.; Li, J.; Zhao, M.; Chen, Z.; Zhang, X.; Li, J. Effects of Surface-Modified MgO Nanoparticles on Inclusion Characteristics and Microstructure in Carbon Structural Steel. *JOM* **2018**, *70*, 1136–1142. [CrossRef]
24. Qu, T.; Wang, D.; Wang, H.; Hou, D.; Tian, J. Thermodynamic analysis on tin precipitation behavior in Ti-bearing peritectic steel after magnesium treatment. *J. Cent. South Univ.* **2020**, *27*, 3637–3651. [CrossRef]
25. Liu, Y.; Zong, N. Effects of Al-Mg alloy treatment on behavior and size of inclusions in SUH 409L stainless steel. *Metall. Res. Technol.* **2018**, *115*, 111. [CrossRef]
26. Park, J.S.; Park, J.H. Effect of Mg-Ti deoxidation on the formation behavior of equiaxed crystals during rapid solidification of iron alloys. *Steel Res. Int.* **2014**, *85*, 1303–1309. [CrossRef]
27. Kim, S.K.; Suito, H.; Inoue, R. Effect of multi-phase oxide particles on TiN crystallization and solidification structure in Ti-added ferritic stainless steel. *ISIJ Int.* **2012**, *52*, 1935–1944. [CrossRef]
28. Wu, Z.; Zheng, W.; Li, G.; Matsuura, H.; Tsukihashi, F. Effect of inclusions' behavior on the microstructure in Al-Ti deoxidized and magnesium-treated steel with different aluminum contents. *Metall. Mater. Trans. B* **2015**, *46*, 1226–1241. [CrossRef]
29. Ma, W.J.; Bao, Y.P.; Zhao, L.H.; Wang, M. Control of the precipitation of TiN inclusions in gear steels. *Int. J. Min. Met. Mater.* **2014**, *21*, 234–239. [CrossRef]
30. Gao, T.; Sun, Z.; Xue, H.; Retraint, D. Effect of surface mechanical attrition treatment on high cycle and very high cycle fatigue of a 7075-T6 aluminium alloy. *Int. J. Fatigue* **2020**, *139*, 105798. [CrossRef]
31. Hultman, L.; Hesse, D.; Chiou, W.A. Mg–Ti–spinel formation at the TiN/MgO interface by solid state reaction: Confirmation by high-resolution electron microscopy. *J. Mater. Res.* **1991**, *6*, 1744–1749. [CrossRef]
32. Qu, T.; Zhang, C.; Wang, D.; Zhan, J.; Tian, J.; Hou, D. Effect of Mg–Ti Treatment on Nucleation Mechanism of TiN Inclusions and Ferrite. *Metals* **2020**, *10*, 755. [CrossRef]
33. Park, J.; Kim, D.; Park, J.H. TEM characterization of a TiN-$MgAl_2O_4$ epitaxial interface. *J. Alloys Compd.* **2017**, *695*, 476–481. [CrossRef]
34. Chowdhury, P.; Sehitoglu, H. Mechanisms of fatigue crack growth–a critical digest of theoretical developments. *Fatigue Fract. Eng. M* **2016**, *39*, 652–674. [CrossRef]
35. Gao, C.; Yang, M.Q.; Pang, J.C.; Li, S.X.; Zou, M.D.; Li, X.W.; Zhang, Z.F. Abnormal relation between tensile and fatigue strengths for a high-strength low-alloy steel. *Mater. Sci. Eng. A* **2022**, *832*, 142418. [CrossRef]
36. Pang, J.C.; Li, S.X.; Wang, Z.G.; Zhang, Z.F. General relation between tensile strength and fatigue strength of metallic materials. *Mater. Sci. Eng. A* **2013**, *564*, 331–341. [CrossRef]

37. Giri, S.K.; Bhattacharjee, D. Fatigue behavior of thin sheets of DP590 dual-phase steel. *J. Mater. Eng. Perform.* **2012**, *21*, 988–994. [CrossRef]
38. Furuya, Y.; Abe, T. Effect of mean stress on fatigue properties of 1800 MPa-class spring steels. *Mater. Des.* **2011**, *32*, 1101–1107. [CrossRef]
39. He, J.; Zhu, S.; Luo, C.; Niu, X.; Wang, Q. Size effect in fatigue modelling of defective materials: Application of the calibrated weakest-link theory. *Int. J. Fatigue* **2022**, *165*, 107213. [CrossRef]
40. Li, X.; Zhu, S.; Liao, D.; Correia, J.A.F.O.; Berto, F.; Wang, Q. Probabilistic fatigue modelling of metallic materials under notch and size effect using the weakest link theory. *Int. J. Fatigue* **2022**, *159*, 106788. [CrossRef]
41. Li, S.; Kang, Y.; Kuang, S. Effects of microstructure on fatigue crack growth behavior in cold-rolled dual phase steels. *Mater. Sci. Eng. A* **2014**, *612*, 153–161. [CrossRef]
42. Zhao, Z.P.; Qiao, G.Y.; Liao, B.; Xiao, F.R. Study of fatigue crack propagation behaviour for dual-phase X80 pipeline steel. *Ironmak. Steelmak.* **2018**, *45*, 635–640. [CrossRef]
43. Song, C.; Wang, H.; Sun, Z.; Wei, Z.; Yu, H.; Chen, H.; Lu, J. Effect of multiphase microstructure on fatigue crack propagation behavior in TRIP-assisted steels. *Int. J. Fatigue* **2020**, *133*, 105425. [CrossRef]